

Reprint  
IN-29

NMF/ISS ACT

035 359

## Melt Convection Effects in the Bridgman Crystal Growth of an Alloy under Microgravity Conditions

**James E. Simpson and Suresh V. Garimella**  
Department of Mechanical Engineering  
University of Wisconsin-Milwaukee  
Milwaukee, Wisconsin 53201

**Henry C. de Groh III**  
NASA Lewis Research Center  
Cleveland, Ohio 44135

**Reza Abbaschian**  
Department of Materials Science and Engineering  
University of Florida  
Gainesville, Florida 32611

### ABSTRACT

The solidification of a dilute alloy (bismuth-tin) under Bridgman crystal growth conditions is investigated in support of NASA's MEPHISTO space shuttle flight experiment. Computations are performed in two-dimensions with a uniform grid. The simulation includes the species-concentration, temperature and flow fields, as well as conduction in the ampoule. Fully transient simulations have been performed; no simplifying steady state approximations are used. Results are obtained under microgravity conditions for pure bismuth, and Bi-0.1 at.%Sn and Bi-1.0 at.%Sn alloys. The concentration dependence of the melting temperature is neglected; the solid/liquid interface temperature is assumed to be the melting temperature of pure bismuth for all cases studied. For the Bi-1.0at.%Sn case the results indicate that a secondary convective cell, driven by solutal gradients, forms near the interface. The magnitude of the velocities in this cell increases with time; this causes increasing solute segregation at the solid/liquid interface.

### NOMENCLATURE

A	area
$c_p$	specific heat at constant pressure
C	species concentration, $C^*/C_0^*$
D	species diffusion coefficient
E	energy
f	volume fraction
g	acceleration due to gravity
Gr	Grashof number, $g\beta_T(T_H-T_C)H^3/\nu^2$
$Gr_s$	solutal Grashof number, $g\beta_C C_0^* H^3/\nu^2$
h	ampoule thickness (outside radius - inside radius)
H	ampoule diameter; reference length
i	specific enthalpy
k	thermal conductivity

$k_p$	segregation coefficient
L	length of simulation domain
$L_A$	translating zone length
Le	Lewis number, $\alpha/D$
Pr	Prandtl number, $\nu/\alpha$
$\vec{q}$	combined convection and diffusion heat flux vector
$\vec{q}_c$	combined convection and diffusion mass flux vector
$rhs_{ij}$	coefficient matrix in equation (20)
$RHS_{ij}$	coefficient matrix in equation (15)
t	time
T	temperature
u,v,w	velocities in the x, y, z directions

### Greek Symbols

$\alpha$	thermal diffusivity
$\alpha_{ij}$	coefficient matrix in equation (20)
$\beta$	expansion coefficient
$\gamma$	solidification front orientation
$\lambda$	nondimensional temperature, $c_p^*(T-T_m)/\Delta H$
$\Delta T$	temperature difference, $T_H - T_C$
$\Delta H$	enthalpy of freezing
$\zeta$	vorticity
$\theta$	nondimensional temperature, $(T-T_C)/(T_H-T_C)$
$\Lambda_{ij}$	coefficient matrix in equation (20)
$\mu$	dynamic viscosity
$\rho$	density
$\phi$	nondimensional enthalpy, $(i - i_m)/\Delta H$
$\psi$	stream function

### Subscripts

0	initial condition
C	cold furnace temperature condition

AIAA/ASME Joint Thermophysics and Heat Transfer Conf.  
Albuquerque, New Mexico, June 1998.

H	hot furnace temperature condition
i, j	located at i, j th finite volume center
I, J	located at I, J th finite difference mesh point
L	liquid
m	at solidification front
mix	mixture
S	solid
w	ampoule wall

#### Superscripts

^	unit vector
~	vector
*	reference or dimensional quantity
n	time step n

## INTRODUCTION

The synthesis of advanced materials, especially for electronics and biomedical applications, demands high-quality crystals. The compositional uniformity (and hence the quality) of such crystals can be profoundly influenced by the transport phenomena which occur in the melt during solidification. The primary transport mechanism causing these deleterious effects is natural convection. The low-gravity environment of space offers an opportunity to suppress the strength of this natural convection. Hence there is a great deal of interest in the study of directional solidification of crystals in space.

The MEPHISTO project (Abbaschian et al. 1992) is a collaborative program of space experiments aimed at understanding the fundamental processes involved in crystal growth. The space-borne experimental apparatus is a Bridgman-type furnace with an isothermal hot zone, an isothermal chill zone, and an insulated gradient zone. The MEPHISTO furnace contains three ingots of Bi-Sn or Sn-Bi binary alloy inside fused silica ampoules with a maximum 6 mm inner diameter and a 10 mm outer diameter. All three samples are solidified simultaneously, under identical thermal conditions. After flight, the samples are extracted and subjected to post-flight analysis. Four MEPHISTO space experiments have taken place previously; the most recent, MEPHISTO-4, flew in November 1997. The MEPHISTO-2 and -4 experiments examined the faceted solidification of bismuth doped with tin (Bi-Sn).

The MEPHISTO-2 experiments studied a Bi-0.1 at.% Sn alloy, with the principal aims being: (i) to examine the interfacial morphological stability threshold of the faceted solid/liquid interface in the absence of convection; (ii) to evaluate the effects of interface kinetics on stability during diffusive, fast diffusive and convective transport regimes; (iii) to examine Bi growth kinetics as a function of supercooling and (iv) to investigate phenomena associated with kinetic roughening (Abbaschian et al. 1992). The experimental data from this mission resulted in a greater understanding of the dominant role of interface kinetics on morphological stability. Stability phenomena were observed that had not been previously predicted by theory or measured in terrestrial experiments (Abbaschian 1996).

The MEPHISTO-4 experiment builds on the results of the MEPHISTO-2 experiment. MEPHISTO-4 used a Bi-1.0 at.% Sn alloy. Modifications to the experimental apparatus included the addition of a 2 mm inner diameter capillary tube that extends half-way through the process zone.

The MEPHISTO project includes a program of computational modeling of the crystal growth process. In particular, the role of convection, which is crucial to a complete understanding of the process, is to be investigated. Since accurate experimental determination of

convection in metallic melts is very difficult to achieve, due to the opacity and chemical reactivity of the melts, convective levels are determined numerically. Furthermore, the computational models themselves are to be improved by a process involving prediction of, and comparison with, the experimental results. The aim of this procedure is to develop effective fully three-dimensional computer simulations of fluid flow related effects (Abbaschian 1996). Previously, three-dimensional solutions for Bridgman growth have been limited to steady-state growth in succinonitrile, a widely used transparent phase change material with properties analogous to metallic materials (Yao and de Groh 1993, de Groh and Yao 1994).

As part of pre-flight computational analysis in support of MEPHISTO-4, convection effects at microgravity levels and the influence of the 2 mm diameter growth capillary have been modeled by means of a transient, 2D FIDAP finite-element model (Yao et al. 1997). A fixed-grid approach was used, with the enthalpy method being employed to model the phase change. Temporal averaging was used for the apparent heat capacity in the discretized equations. Due to computational difficulties introduced by the small partition coefficient for Bi-Sn, the presence of solute was ignored.

Preliminary scaling arguments of the convection levels by de Groh and Nelson (1994) imply that solutal convection effects on solute segregation may be significant. However, thus far, it has not been possible to include solutal convection, or even a passive solute, into numerical simulations involving phase change for MEPHISTO-4. This is due to the difficulties concerning convergence with front-tracking methods as well as those imposed by the low value of the partition coefficient for Bi-Sn (Yao et al. 1995, Yao et al. 1997, Simpson et al. 1998).

Many simulations of Bridgman crystal growth processes, both under terrestrial and microgravity conditions, are available in the literature. The majority of these simulations can be classified as *pseudo steady state* models (PSSM). The key assumption in such models is that a "steady state" mode of alloy solidification exists, i.e. the concentration of the dopant in the solid which forms at the interface is equal to the initial dopant concentration in the liquid (Kurz and Fisher 1989). Such models vary in complexity from simple 2D analyses that consider the interface to be flat (Alexander et al. 1989, Yao et al. 1995, Simpson et al. 1998) to much more complex formulations that are able to handle interface curvature and wall conduction (Adornato and Brown 1987) and fully three dimensional simulations (Yao and de Groh 1993, Liang and Lan 1996). However, because of the low partition coefficient for Bi-Sn alloys, a "steady state" mode of solidification is never achieved during the MEPHISTO experiments. Thus pseudo steady state models are not appropriate; fully transient simulations need to be developed in order to faithfully model this process.

The computational modeling presented in this paper is intended to examine the effects of thermosolutal natural convection on the MEPHISTO-4 solidification experiments. This will be achieved using a fully transient 2D model, which includes most of the effects of binary alloy solidification and convection driven by both thermal and solutal gradients. Conduction through the ampoule wall will be considered, while the capillary tube and the dependence of melting temperature on concentration will be ignored. For the purposes of our model, we assume that the liquid/solid interface remains distinct like that for a pure material.

## MATHEMATICAL FORMULATION

The problem under consideration is the directional solidification of a binary alloy by the Bridgman process, as shown schematically in Fig. 1.

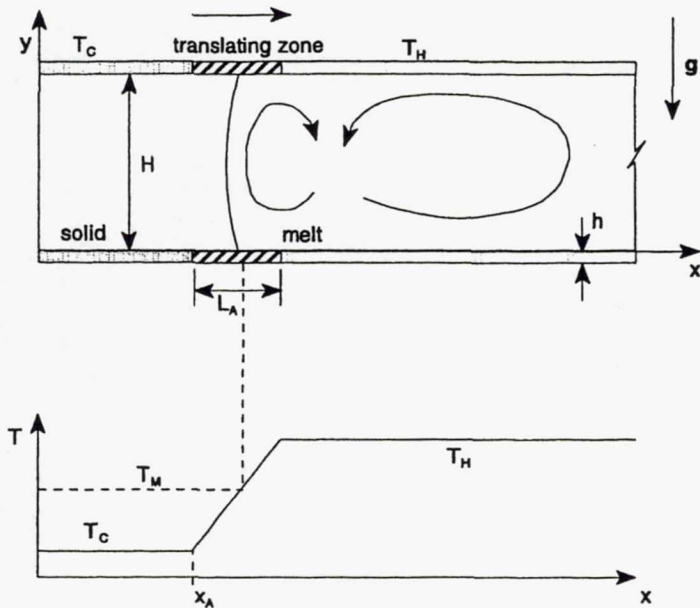


Fig. 1. Schematic of the Bridgman crystal growth process and furnace temperature profile.

The gravity vector is perpendicular to the furnace axis (horizontal Bridgman growth configuration). The melt region is considered to be a viscous Newtonian fluid subject to thermosolutal convection. Thermophysical properties are considered as constant but distinct for the solid and liquid phases. Density variations are considered to be subject to the Boussinesq approximation. The governing equations for the velocity field are the vorticity and vector potential equations which, in nondimensionalized form, are (Mallinson and de Vahl Davis 1973):

$$\frac{\partial \zeta}{\partial t} + \nabla \times (\zeta \times \bar{u}) = -Gr(\nabla \times \hat{g}) - Gr_s(\nabla \times C \hat{g}) + Pr \nabla^2 \zeta \quad (1)$$

$$\nabla^2 \psi = -\zeta \quad (2)$$

In these equations, the definition of vorticity and the relationship between velocity and vector potential are

$$\zeta = -\nabla \times \bar{u}, \quad \bar{u} = \nabla \times \psi \quad (3)$$

In the nondimensionalization, the ampoule inside diameter  $H$ , is selected to be the reference length. The characteristic time and velocity become  $t^* (= H^2/\alpha)$  and  $v^* (= H/t^* = \alpha/H)$ .

The solution of equation (1) subject to equation (2) constitutes the vorticity-vector potential formulation for natural convection. For a non-slip wall, the boundary conditions to be imposed on vorticity and vector potential (Mallinson and de Vahl Davis 1973) are that the velocity is zero, as are the tangential derivatives of its components. This leads to the following conditions for vorticity

$$\begin{aligned} \zeta_1 &= 0 \\ x=0 \quad \zeta_2 &= -\frac{\partial w}{\partial x} \\ \zeta_3 &= \frac{\partial v}{\partial x} \end{aligned} \quad (4)$$

The vector potential at a plane, impermeable surface is normal to the surface and its gradient is zero:

$$\begin{aligned} \frac{\partial \psi_1}{\partial x} &= 0 \\ x=0 \quad \psi_2 &= 0 \\ \psi_3 &= 0 \end{aligned} \quad (5)$$

The boundary conditions for the other surfaces result from similar considerations (Mallinson and de Vahl Davis 1973). As an initial condition, the fluid must be quiescent

$$t=0 \quad \psi = \zeta = 0. \quad (6)$$

The nondimensionalized form of the governing equation for the conservation of energy is

$$\frac{\partial \theta}{\partial t} + \nabla \cdot (\bar{u} \theta) = \nabla^2 \theta \quad (7)$$

It will be seen below that an integral form of this equation is suitable for calculating phase-change. An initial temperature equal to the hot wall temperature is applied throughout the flow field. The boundary conditions at the  $x=0$  and  $x=L$  walls are shown in Fig. 1.

The thermal boundary conditions along the  $y=-h$  and  $y=H+h$  walls required for the Bridgman process need closer examination, since they are a function of time. A schematic of the temperature imposed at these boundaries, which approximates the furnace, is shown in Fig. 1. There is a translating zone (considered an "adiabatic" zone if the temperature profile is unknown) between the hot and cold regions of the furnace, in which the temperature linearly increases from the cold furnace temperature to the hot furnace temperature. The melting temperature of the material occurs somewhere within this zone, which translates with time at a constant  $x$ -velocity, known as the *translation velocity*,  $u_t$ . This is what facilitates the directional growth of the crystal. Defining the  $x$  location where the translating zone meets the cold furnace temperature zone to be at  $x_A(t)$ , the boundary condition for temperature may be expressed as

$$\text{at } y = -h, H+h: T = \begin{cases} T_c, & \text{for } x < x_A(t) \\ T_c + \Delta T \frac{x - x_A(t)}{L_A}, & \text{for } x_A(t) \leq x \leq [x_A(t) + L_A] \\ T_h, & \text{for } x_A(t) < x \end{cases} \quad (8)$$

In principle, the solution of the energy equation (7) coupled with the solution of the vorticity-vector potential equations (1), (2) and (3) would yield the temperature and velocity distribution throughout the simulation domain. However, the problem of modeling the physics of the propagation of the solidification front and determining its location remains to be addressed. We choose to do this by the enthalpy method (Alexiades and Solomon 1993). The constitutive equation required for this method is the integral equation describing the conservation of energy in an arbitrary control volume:

$$\int_t^{t+\Delta t} \frac{\partial}{\partial t} \left( \int_V E dV \right) dt = \int_t^{t+\Delta t} \int_A -\bar{q} \cdot \hat{n} dA dt \quad (9)$$

Unlike the differential form of the energy equation (7), equation (9) is valid for any control volume in the solution domain, including control volumes which are intersected by the interface.

The nondimensionalized equation for the conservation of solute throughout the computational domain is

$$\frac{\partial C}{\partial t} + \nabla \cdot (\bar{u} C) = \frac{1}{Le} \nabla^2 C \quad (10)$$

This equation is analogous to the energy equation. We impose an initial

solute concentration throughout the solution domain. At the boundaries we demand that there be no flux of solute: no solute may exit the solution domain. Thus,

$$\begin{aligned} t = 0 & \quad C = C_0 \\ x = 0, L & \quad \partial C / \partial x = 0 \\ y = 0, H & \quad \partial C / \partial y = 0 \end{aligned} \quad (11)$$

Again, in principle, solution of equation (10) along with energy equation (7) and vorticity-vector potential equations (1), (2) and (3) all subject to the relevant boundary and initial conditions are enough to determine the solute, temperature and velocity values throughout the solution domain. However, the more general problem involving phase change demands that the thermodynamics of solute redistribution be addressed. The methodology for this is described in the next section. The constitutive equation for this method uses the integral form of equation (10),

$$\int_t^{t+\Delta t} \frac{\partial}{\partial t} \left( \int_V C_{\text{mix}} dV \right) dt = \int_t^{t+\Delta t} \int_A -\bar{q}_c \cdot \hat{n} dA dt \quad (12)$$

## NUMERICAL ANALYSIS

The computational domain is primarily discretized using regularly spaced finite difference mesh points. Superimposed on this grid are finite volumes which are required for the enthalpy method. The finite-volume centers are staggered with respect to the finite-difference mesh point locations. Vorticity, velocity and vector potential are calculated at the finite difference mesh points. Temperature, solute concentration and enthalpy are evaluated at the control volume centers as a result of the solution of equations (9) and (12).

The discretization and the accompanying solution scheme are explained in Simpson and Garimella (1997). The approach used here is modified from a program (Timchenko et al. 1997) written for the solution of natural convection in a rectangular cavity. The essential details are that the vorticity transport equation (1) and the vector potential equation (2) are discretized in space using the regular finite difference mesh. The discretized equation for the vorticity transport equation is solved using an Alternating Direction Implicit (ADI) scheme (Samarskii and Andreyev 1963). The discretized equation for vector potential is solved using the conjugate gradient method. This is a semi-iterative method used to solve specific systems of linear equations. The method is not discussed here, except to note that the values for vector potential at the previous time step are used as the initial guess values. Once the values of vector potential are known, the nodal velocities can be determined from equation (3).

It should be noted that while governing equations (1) and (2) are presented in three dimensions and the code is capable of solving for the flow field in 3D, the simulations in this paper are restricted to two dimensions. This is accomplished by solving only the z-component of vorticity and vector potential and thus yielding the requisite u- and v-velocity components.

The discretization for the boundary conditions on vorticity (4) and vector potential (5) at a wall aligned with the Cartesian grid are easy to realize. However, the boundary conditions at the arbitrarily oriented interface require special handling. The slope of the interface is found using a Hirt and Nichols (1981) type front reconstruction; the boundary conditions may then be applied (following Raw and Lee 1991, Roache 1976) as:

$$\psi_3 = 0 \quad \zeta_3 = (\cos^{-2} \gamma) \partial^2 \psi_3 / \partial y^2 = (\sin^{-2} \gamma) \partial^2 \psi_3 / \partial x^2 \quad (13)$$

The slope of the interface is used to determine which of the two formulations for vorticity at the boundary is used. If the line is more horizontal than vertical then the first formulation is used and the converse applies.

The integral energy equation (9) is discretized using the finite volume mesh. An upwind scheme is incorporated for the treatment of convective heat fluxes. This discretization may then be written as

$$\begin{aligned} \frac{\phi_{ij}^{n+1} - \phi_{ij}^n}{\Delta t} \Delta x \Delta y = & \Delta y \left[ \lambda_{ij}^{n+1} [u_{i-\frac{1}{2},j}, 0] - \lambda_{i-1,j}^{n+1} [-u_{i-\frac{1}{2},j}, 0] + \lambda_{ij}^{n+1} [u_{i+\frac{1}{2},j}, 0] - \lambda_{i+1,j}^{n+1} [u_{i+\frac{1}{2},j}, 0] \right] \\ & + \Delta x \left[ \lambda_{ij}^{n+1} [v_{i,j-\frac{1}{2}}, 0] - \lambda_{i,j-1}^{n+1} [-v_{i,j-\frac{1}{2}}, 0] + \lambda_{ij}^{n+1} [v_{i,j+\frac{1}{2}}, 0] - \lambda_{i,j+1}^{n+1} [v_{i,j+\frac{1}{2}}, 0] \right] \quad (14) \\ & + \Delta y \left[ k_{i+\frac{1}{2},j} (\lambda_{i+1,j}^{n+1} - \lambda_{i,j}^{n+1}) / \Delta x - k_{i-\frac{1}{2},j} (\lambda_{i,j}^{n+1} - \lambda_{i-1,j}^{n+1}) / \Delta x \right] \\ & + \Delta x \left[ k_{i,j+\frac{1}{2}} (\lambda_{i,j+1}^{n+1} - \lambda_{i,j}^{n+1}) / \Delta y - k_{i,j-\frac{1}{2}} (\lambda_{i,j}^{n+1} - \lambda_{i,j-1}^{n+1}) / \Delta y \right] \end{aligned}$$

in which [A, B] is the maximum of A and B. The velocities at the finite volume faces are the interpolated values from the finite-difference mesh points.

The *modified enthalpy method* is the solution scheme for the energy equation. The thrust of the method is to use equation (9) to determine the cell temperature and enthalpy. The complete methodology for the solution is explained in Simpson and Garimella (1997); an explanation of the modifications necessary to account for the presence of the ampoule wall is provided in Garimella and Simpson (1998). Essentially, equation (14) is advanced forward in time using Gauss-Seidel iteration with successive over relaxation. For this method, equation (14) reduces to

$$\phi_{ij}^{p+1} + C_{ij}^p \lambda_{ij}^{p+1} = \text{RHS}_{ij}^p \quad (15)$$

in which p denotes the inner iteration number and the RHS matrix is fully explicit at iteration p. The values at time step n are used as the first approximation. In the melt region or in the solid, the relationship between temperature and enthalpy gives us

$$\phi_{ij}^{p+1} = \begin{cases} \frac{\text{RHS}_{ij}^p}{C_{ij}^p + c_{ps}}, & \text{if } \text{RHS}_{ij}^p \leq 0 \\ 0, & \text{if } 0 < \text{RHS}_{ij}^p < 1 \\ \frac{\text{RHS}_{ij}^p + C_{ij}^p}{C_{ij}^p + c_{pl}}, & \text{if } \text{RHS}_{ij}^p \geq 1 \end{cases} \quad (16)$$

with corresponding results for the temperature ( $\lambda$ ). The scheme is modified in the manner explained in Garimella and Simpson (1998) so that it is also valid for the ampoule wall region and furnishes the temperatures in that region without any special handling. Iterations proceed until convergence, at which time the new values at time step n+1 for temperature and enthalpy are declared to be those found at convergence. Convergence is assessed by examining the change in the solution and the change in the solution residual with a tolerance of  $10^{-6}$  (Garimella and Simpson 1998, Barrett et al. 1994). In cells which contain the interface, the cell enthalpies are equivalent to the cell liquid fractions by virtue of our nondimensionalization scheme. This allows the front orientation to be determined using Hirt and Nichols (1981). The front orientations are required for the calculation of vorticity at the interface.

The discretized analog of equation (12) is

$$\begin{aligned}
& \frac{C_{mix,ij}^{n+1} - C_{mix,ij}^n}{\Delta t} \Delta x \Delta y = \\
& \Delta y \left[ C_{L,ij}^{n+1} [u_{i-\frac{1}{2},j}, 0] - C_{L,i-1,j}^{n+1} [-u_{i-\frac{1}{2},j}, 0] \right] \\
& + \Delta y \left[ C_{L,ij}^{n+1} [-u_{i+\frac{1}{2},j}, 0] - C_{L,i+1,j}^{n+1} [u_{i+\frac{1}{2},j}, 0] \right] \\
& + \Delta x \left[ C_{L,ij}^{n+1} [v_{i,j-\frac{1}{2}}, 0] - C_{L,i,j-1}^{n+1} [-v_{i,j-\frac{1}{2}}, 0] \right] \\
& + \Delta x \left[ C_{L,ij}^{n+1} [-v_{i,j+\frac{1}{2}}, 0] - C_{L,i,j+1}^{n+1} [v_{i,j+\frac{1}{2}}, 0] \right] \\
& + \frac{1}{Le} \Delta y \left[ D_{i+\frac{1}{2},j} \frac{C_{L,i+1,j}^{n+1} - C_{L,ij}^{n+1}}{\Delta x} - D_{i-\frac{1}{2},j} \frac{C_{L,ij}^{n+1} - C_{L,i-1,j}^{n+1}}{\Delta x} \right] \\
& + \frac{1}{Le} \Delta x \left[ D_{i,j+\frac{1}{2}} \frac{C_{L,i,j+1}^{n+1} - C_{L,i,j}^{n+1}}{\Delta y} - D_{i,j-\frac{1}{2}} \frac{C_{L,i,j}^{n+1} - C_{L,i,j-1}^{n+1}}{\Delta y} \right]
\end{aligned} \quad (17)$$

The assumptions made in arriving at this equation are that the densities of the liquid and solid phases are constant and equal, so that a simple mixture rule applies, and that there is no diffusion in the solid (except in the cells that contain the interface, in which the equilibrium lever rule is assumed); the concentration at which the solute first solidifies is the concentration at which that portion of solid remains for all time.

Solution of this finite volume equation is explained in Simpson and Garimella (1998). For the purposes of our model, we assume that there is no effect of concentration on the melting temperature and the liquid/solid interface remains distinct like that for a pure material. The significant result of this assumption is that the enthalpy method is decoupled from the concentration equation and is the only mechanism necessary to determine the location of the solidification front.

The LHS of equation (17) may be expressed in terms of liquid solute concentration,  $C_L$  as

$$\frac{[C_{mix,ij}^{n+1} - C_{mix,ij}^n]}{\Delta t} \Delta x \Delta y = \frac{[f_L^n C_L^{n+1} - \alpha_{ij}^n C_L^n]}{\Delta t} \Delta x \Delta y \quad (18)$$

in which

$$\alpha_{ij}^n = [(k_p - 1)f_L^{n+1} + (2 - k_p)f_L^n]$$

and this is known at time step  $n$  since the liquid fractions at  $n+1$  are recovered directly from the solution of the energy equation. The solute concentration in the solid portion of a node may be found from employing the relation

$$C_S^{n+1} = \frac{C_S^n f_S^n + k_p C_L^n (f_L^{n+1} - f_L^n)}{f_S^{n+1}} \quad (19)$$

The discretized equation (17), subject to (18) is solved by Gauss-Seidel iteration in a manner analogous to the energy equation, i.e.,

$$[\alpha_{ij}^p + \Lambda_{ij}^p] C_{L,ij}^{p+1} = rhs_{ij}^p \quad (20)$$

The solution scheme for simplified, fully transient solidification in two-dimensional Bridgman crystal growth subject to thermosolutal convection has now been fully specified.

## RESULTS AND DISCUSSION

### Pure Bismuth

Simulations for the Bridgman crystal growth of pure bismuth were performed. Thermophysical properties from Yao et al. (1995) were used.

The cold and hot furnace temperatures were  $T_C = 50^\circ\text{C}$  and  $T_H = 700^\circ\text{C}$  respectively. Liquid properties were used as the reference properties for the nondimensionalization scheme. The properties for solid and liquid bismuth were evaluated at the mean solid and the mean liquid temperatures of  $160.7^\circ\text{C}$  and  $485.7^\circ\text{C}$ , respectively. The reference density was considered to be equal for both phases. The property values were:  $k_s = 6.872 \text{ W/mK}$ ,  $k_l = 14.66 \text{ W/mK}$ ,  $\rho_0 = 10,070 \text{ kg/m}^3$ ,  $c_{ps} = 132.6 \text{ J/kgK}$ ,  $c_{pl} = 135.3 \text{ J/kgK}$ ,  $\Delta H = 52.3 \text{ kJ/kg}$ ,  $\mu = 1.240 \times 10^{-3} \text{ Ns/m}$  and  $T_m = 271.3^\circ\text{C}$ . The thermal expansivity of the liquid was taken to be  $\beta_T = -1.25 \times 10^{-4} \text{ K}^{-1}$ . The properties used for the alumina ampoule wall were  $k_w = 2.10 \text{ W/mK}$ ,  $\rho_w = 2,020 \text{ kg/m}^3$ ,  $c_{pw} = 92.10 \text{ J/kgK}$  (In the MEPHISTO flight experiments, a fused silica ampoule is used, which has a higher value for specific heat. This is not expected to have a significant impact on the results. In future work, fused silica properties will be employed). The dimensions used to define the domain were  $H = 6 \text{ mm}$  and  $L = 73 \text{ mm}$ . The ampoule wall thickness,  $h$ , was  $2 \text{ mm}$ . The length of the insulated translating zone was  $L_A = 25 \text{ mm}$ , with a translation velocity of  $u_t = 3.38 \mu\text{m/s}$ . The gravity level was  $10 \mu\text{g}$ , with gravity acting in the negative  $y$  direction. The important nondimensional quantities from these values are  $Gr = 113.6$  and  $Pr = 0.01144$ . In order to start the crystal growth simulations, the following procedure was carried out in each simulation. The initial position of the translating zone was flush with the  $x = 0$  wall. This zone is immobilized for the first 5,000 time steps. During this time, the velocity and concentration field solution schemes are switched off while solid rapidly chills in the portion of the translating zone which is lower than the melting temperature. After this, simulations proceed with the entire solution scheme enabled, and the insulated zone moving at the translation velocity  $u_t$ .

The computational domain was discretized by means of a regularly spaced  $200 \times 28$  mesh, with 20 of the 28  $y$ -direction cells being in the sample and the remaining 8 in the ampoule walls. This mesh was selected as a result of numerical experiments which indicated its adequacy in resolving solute gradients in the liquid near the interface. The temporal step size was  $\Delta t = 6.25 \times 10^{-2}$ . The program was written in ANSI standard FORTRAN 77 and implemented on a DEC 3000/700 (225 MHz, SPECfp95 5.71). The total CPU requirement for 61,000 time steps was 4.33 hours. Note the efficiency of the method even with the fine mesh.

Figure 2 (a) shows a plot of velocity vectors and isotherms after 19,000 time steps (0.81 hours) have elapsed. Isotherms are shown in the ampoule wall as well as in the liquid and solid bismuth. The thick line at  $x \approx 3.15$  represents the solid/liquid interface. The dominant feature of this plot is the counter-clockwise convective cell in the translating zone ( $3.15 < x < 7.8$ ). For clarity, velocity vectors are plotted on every other mesh point in the  $x$ -direction in this figure. The maximum (nondimensional) velocity in this convective cell is  $1.936 \times 10^{-3}$  at  $(4.625, 0.2)$ . The ratio of this velocity to the translation velocity,  $u_t$ , is 1.08, which compares well with the value of 1.12 found using a finite-element, variable-property simulation of the same process by Yao et al. (1997). Velocities in the negative  $y$ -direction at the interface are constrained and concentrated by the presence of the solid whereas velocities in the positive  $y$ -direction at the opposite (hot) end of the translating zone are much more diffuse.

The other main feature of this plot is the isotherms throughout the solution domain. On the outside edge of the ampoule, the (imposed) temperature profile is a linear ramp function within the translating zone. This is easily witnessed by the regularly spaced isotherms on the outer edge. In the ampoule region, the isotherms are dramatically distorted. Since the ampoule material has a low thermal conductivity, the thermal

field on the inside of the ampoule wall differs from that imposed on the outside. For  $x \leq 4.4$ , the temperature in the ampoule is greater than the applied temperature (note the isotherms distort sharply to the left). For  $x \geq 4.4$ , the converse is true. In the bismuth region the isotherms exhibit the same trend, and have a gentle, crescent-shaped curvature. The isotherms and the interface appear to be symmetric about the centerline ( $y = 0.5$ ) and thus have not been discernibly influenced by convective transport in the melt.

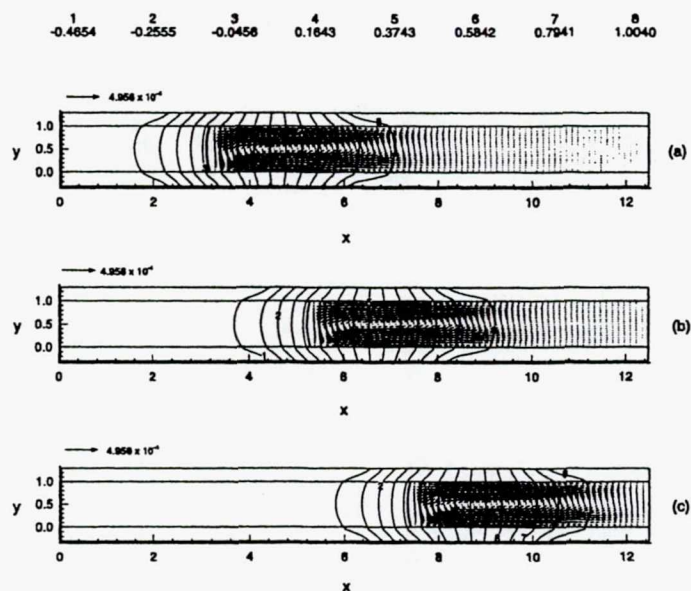


Fig. 2. Velocity vectors and isotherms for the Bridgman growth of pure bismuth at (a) 19,000 time steps (0.81 hours), (b) 37,000 time steps (1.63 hours) and (c) 55,000 time steps (2.90 hours). The solid line indicates the location of the solid/liquid interface. The velocity vectors, shown at every other location in the  $x$ -direction, indicate a single, counter-clockwise convective cell.

Figures 2 (b) and 2 (c) are plots of velocity vectors and isotherms at 37,000 (1.63 hours) and 55,000 time steps (2.90 hours), respectively. The progression of the translating zone (and thus of the solidification front) is obvious from these figures. After 1.63 hours, the front is at  $x \approx 5.2$ , and the nature of the convective motions is unchanged. The magnitude of the maximum velocity is identical to that at the previous time (Fig. 2a), and its new location is (6.6875, 0.2). At a still later time (2.90 hours), when the front is at  $x \approx 7.4$ , the velocity increases slightly to  $1.943 \times 10^{-3}$  and is at (8.8125, 0.2). This indicates that end effects are coming into play, and so, results after this point are not considered.

Figure 3 is a trace of temperatures at three different  $y$ -locations, 1.63 hours into the process (Fig. 2b). The solid line ( $y = 1.2917$ ) is the applied thermal boundary condition. The  $y = 1.0$  trace is along the inside of the ampoule wall. These two traces are significantly different, indicating the need to include the ampoule wall in the simulation. The third trace ( $y = 0.5$ ) is the temperature along the centerline of the domain. Note the change in slope at the solidification front (at  $x = 5.2$ ). This is due to the change in material properties in the liquid and solid phases. These results agree well with those found in Yao et al. (1997), both in terms of the temperature values and the slope change due to property variation at the interface.

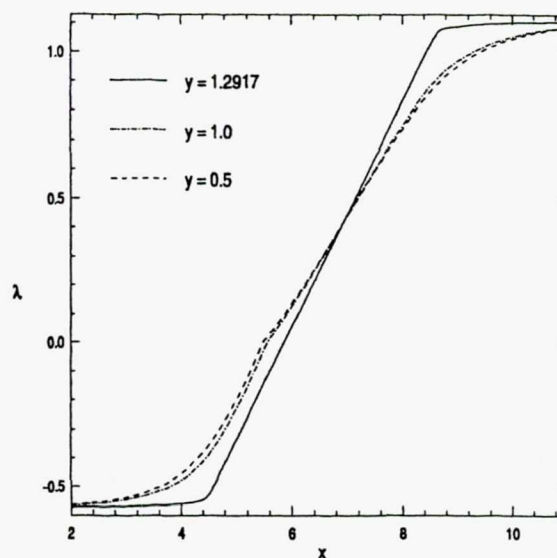


Fig. 3. Temperature traces at  $y = 1.2917$  (the outermost cell in the ampoule),  $y = 1.0$  (along the inside of the ampoule wall) and  $y = 0.5$  (the centerline), for the pure bismuth case after 1.63 hours. The results show the dramatic influence of the ampoule on the thermal field applied to the bismuth sample.

#### Bi-0.1 at. % Sn alloy (MEPHISTO-2)

For simulating the Bridgman crystal growth of a Bi-0.1 at. % Sn alloy, the thermophysical properties used were the same as for the simulation of pure bismuth described above. In addition, the value for diffusivity of liquid Sn in liquid Bi was  $D = 6.22 \times 10^{-9} \text{ m}^2/\text{s}$ , and the partition coefficient was  $k_p = 0.029$ . The value of solutal expansion coefficient was taken to be  $\beta_c = -0.305 \text{ (at. \%)}^{-1}$ . The diffusivity value was calculated at the mean melt temperature. The liquid composition was taken to be at a uniform value of 0.1 at. % as the initial condition. These values result in dimensionless parameters  $Gr_i = 0.4262$  and  $Le = 1730$ . Simulations were performed using the same computer, spatial discretization and time step as for the pure bismuth case. The CPU burden for 60,000 time steps was 4.98 hours.

Velocity vectors and isotherms after 0.81 hours are shown for this alloy in Fig. 4 (a). The nature of the convective flow is similar to that for pure bismuth (Fig. 2a). A single, counter-clockwise, thermally driven convective cell dominates the velocity plot. The maximum  $u$ -velocity is slightly less than for pure bismuth, and is at the same location. However, the magnitude of the maximum  $v$ -velocity is  $9.874 \times 10^{-4}$  at (3.375, 0.5) acting in the negative  $y$  direction, which is lower in magnitude than for pure bismuth ( $1.047 \times 10^{-3}$ ). Solute rejected at the interface acts to oppose the thermally driven convective motion, resulting in retarded velocities near the interface. The thermal field is not distorted by the action of convection. Figure 4 (b) is a plot of velocity vectors and isotherms after 1.63 hours. Again the convective motion and temperature field is similar to the pure bismuth case (Fig. 2b). The magnitude of the maximum  $v$ -velocity has decreased to  $9.527 \times 10^{-4}$  acting downward at (5.5, 0.5) as a result of continuing solute rejection at the interface. At a later time (2.90 hours, Fig. 4c), the maximum  $v$ -velocity is  $9.353 \times 10^{-4}$  at (7.6875, 0.5) confirming the trend of solute rejection opposing the convective motion due to the applied temperature gradient.

1 -0.4671 2 -0.2570 3 -0.0468 4 0.1833 5 0.3735 6 0.5838 7 0.7938 8 1.0039

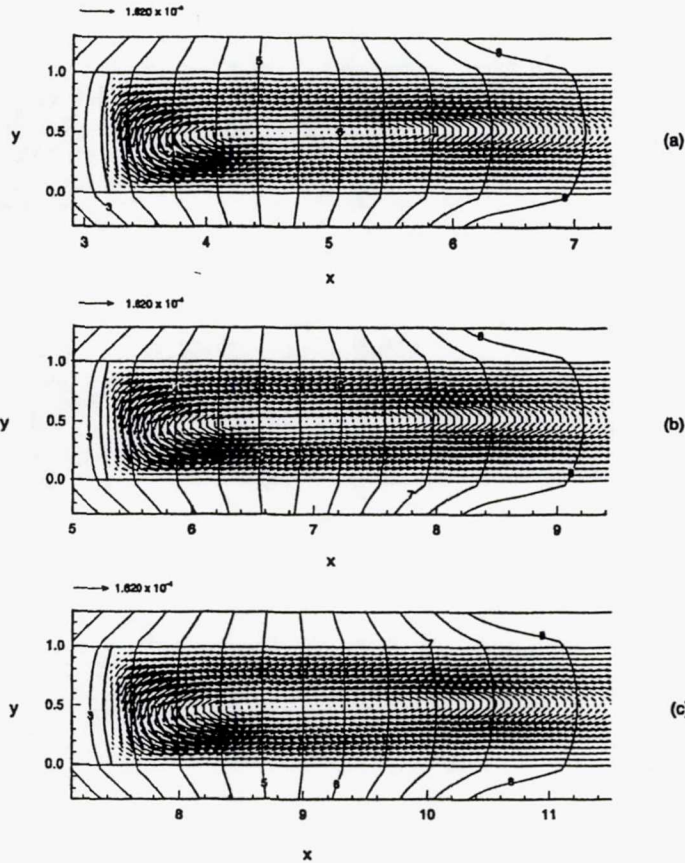


Fig. 4. Velocity vectors and isotherms for the Bridgman growth of Bi-0.1 at.% Sn at (a) 0.81 hours, (b) 1.63 hours, and (c) 2.90 hours. The solid line indicates the location of the solid/liquid interface. A single, counter-clockwise convective cell is present in all cases.

Solute concentrations in the liquid at the same three times as in Fig. 4 are illustrated in Fig. 5. The solute build-up near the interface, and the exponential profile characteristic of binary-alloy solute rejection, are clearly evident. The increased solute concentration levels at small  $y$  result from the convective flow sweeping solute "down" the interface in the direction of decreasing  $y$  and away from the interface in the direction of increasing  $x$  (refer to Fig. 4). Closer to the interface, the solute concentration exhibits a minimum value near  $y = 0.7$ . The minimum value is found at this location for two reasons. The curvature of the interface causes the value at the centerline to be lower than that found at the outside edges. In the absence of convection the minimum value would be expected to occur at  $y = 0.5$ . In addition, the incoming hot, solute-poor liquid in the upper portion of the domain causes this minimum value to be offset to  $y \approx 0.7$ . Note also that the flow near the top is retarded due to the presence of the non-slip wall; this results in increased solute concentration levels there.

1 0.0010 2 0.0019 3 0.0028 4 0.0037 5 0.0046 6 0.0055 7 0.0064 8 0.0073

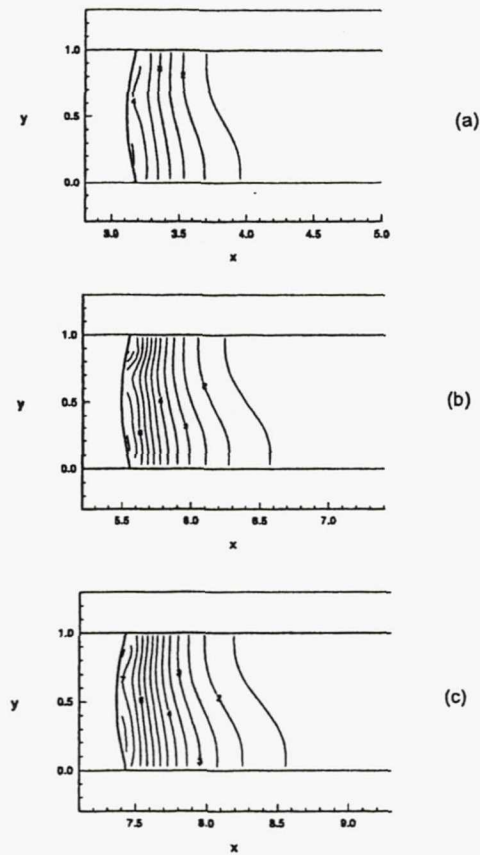


Fig. 5. Liquid solute concentration values for Bi-0.1 at.% Sn at (a) 0.81 hours, (b) 1.63 hours, and (c) 2.90 hours. The profiles are a result of combined diffusive and convective processes. The maximum concentration increases for each case, indicating solute build-up.

In Fig. 5 (a), the extreme values for solute concentration at the first mesh points adjacent to the interface ( $x = 3.1563$ ) are 0.4207 at.% at  $y = 0.175$  and 0.3718 at.% at  $y = 0.675$ . The front is approximately at  $x = 5.2$  after 1.63 hours have elapsed (Fig. 5b). Solute buildup is seen to continue as the front progresses, with the extreme values of liquid solute concentration near the interface ( $x = 5.2813$ ) being 0.5894 at.% at  $y = 0.875$  and 0.5347 at.% at  $y = 0.625$  respectively. Although the maximum value is now near the top of the domain (whereas it was near the bottom in Fig. 5a), the value for solute concentration near the bottom ( $y = 0.275$ ) is still as high as 0.5887 at.%, indicating that solute segregation in the  $y$ -direction is not monotonic. In Fig. 5 (c) the front is at approximately  $x = 7.4$ , and the extreme solute concentrations near the interface ( $x = 7.4063$ ) are 0.7105 at.% at  $y = 0.125$  and 0.6429 at.% at  $y = 0.625$ . Note that these concentration values will not cause a significant change in the melting temperature of the alloy as predicted by the Bi-Sn binary phase diagram. Thus the assumption of a constant melting temperature is valid. Figure 5 shows that the solute levels near the interface increase with time. It appears that this solute build-up is responsible for a corresponding decrease in the convective velocities near the interface with time (refer to the preceding discussion of the velocity field). The presence of solute

near the interface acts to make the fluid less dense. This opposes the action of the thermal field which increases the fluid density near the interface. The net effect is that the thermally driven convection near the interface is retarded by this opposing potential.

For the low-concentration alloy, the liquid solute concentration profiles are governed by solute rejection at the interface and by thermal convection only. The action of solutal convection is limited at these low concentrations. The velocity field indicates that thermal convection decreases slightly with time.

#### Bi-1.0 at.% Sn alloy (MEPHISTO-4)

A richer alloy was simulated next. The liquid composition was taken to be at a uniform value of 1.0 at.% Sn as the initial condition (yielding  $Gr_1 = 4.262$ ). Unlike the previous simulations, computations were performed using a Silicon Graphics Indigo 2 workstation (250 MHZ CPU, SPECfp92 177.5). The CPU burden for 61,000 time steps was 8.27 hours.

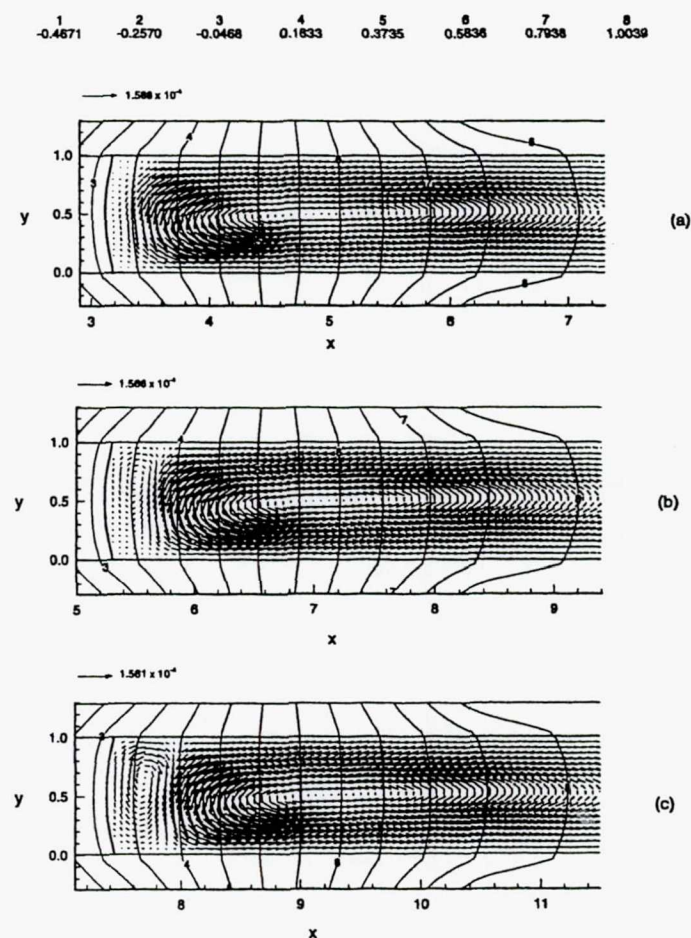


Fig. 6. Velocity vectors and isotherms for the Bridgman growth of Bi-1.0 at.% Sn at (a) 0.81 hours, (b) 1.63 hours, and (c) 2.90 hours. The solid line indicates the location of the solid/liquid interface. A primary counter-clockwise convective cell, driven by thermal gradients, is evident in all three panels. A secondary, clockwise cell, driven by solutal gradients, develops with time.

Velocity vectors and isotherms after 0.81 hours for this alloy are shown in Fig. 6 (a). The velocity vectors indicate a primary convective cell rotating in a counter-clockwise manner in the translating zone. However, the velocities differ from those shown in Figs. 2 (a) and 4 (a); the convective velocities in the region near the interface are significantly smaller in Fig. 6 (a). In fact, there are some *positive*  $v$ -velocities in the region near the interface at  $y \approx 0.9$ . Since these positive velocities are only present at a few mesh points, an organized convective cell driven by solute gradients is not discerned; however, a  $v$ -velocity contour plot (not shown) revealed the presence of a small convective cell. The maximum  $u$ -velocity for this case is  $+1.885 \times 10^{-3}$  at (4.8125, 0.2), which is lower than the value of  $1.936 \times 10^{-3}$  found for pure bismuth. The maximum  $v$ -velocity magnitude is  $7.702 \times 10^{-4}$  acting downward at (3.6875, 0.5), which is also significantly lower than the value of  $1.047 \times 10^{-3}$  for pure bismuth, or the  $9.874 \times 10^{-4}$  value found for Bi-0.1 at.% Sn. Higher levels of solute rejection due to the higher initial concentration of the melt are responsible for these effects.

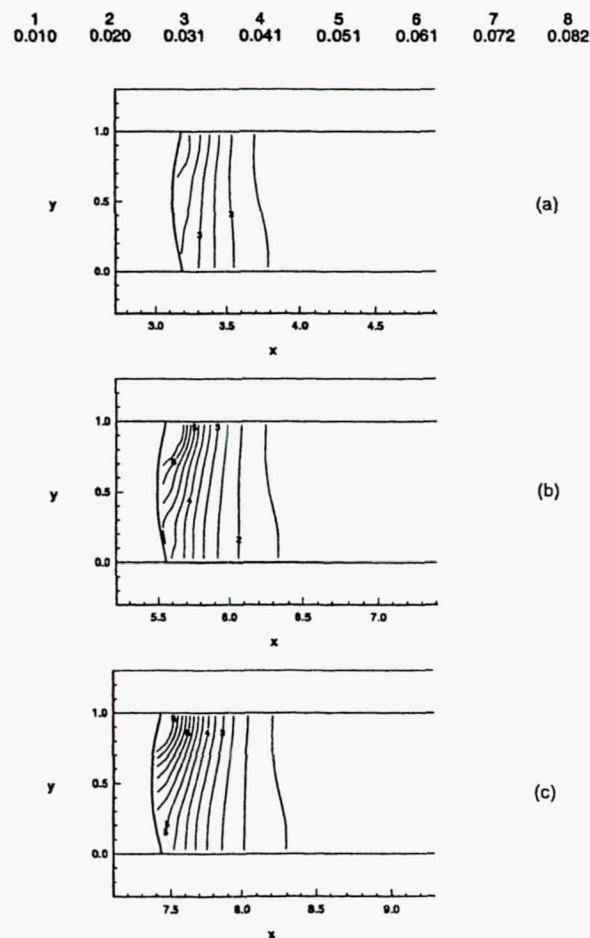


Fig. 7. Liquid solute concentration values for Bi-1.0 at.% Sn at (a) 0.81 hours, (b) 1.63 hours, and (c) 2.90 hours. The profiles are a result of combined diffusive and convective processes. The maximum concentration increases for each case, as does the segregation in the  $y$ -direction.

At a later time (1.63 hours), the front is at  $x \approx 5.4$ , as shown in Fig. 6 (b). A secondary, clockwise convective cell driven by solute gradients has formed adjacent to the interface. The two-cell convective motion is in contrast to that observed in Figs. 2 (b) and 4 (b). The  $v$ -velocities near the interface are positive along the entire interface height. The maximum  $v$ -velocity in the secondary convective cell near the interface at (5.375, 0.7) is  $+2.187 \times 10^{-4}$ , and the maximum  $u$ -velocity in the domain is  $+1.858 \times 10^{-3}$  at (7.0, 0.2). Later in the growth process (2.90 hours), the front has advanced to  $x \approx 7.4$ , and the secondary convective cell has increased in size and strength as solute – the driving force for this cell – continues to build up at the interface. The maximum  $u$ -velocity in the domain is  $+1.852 \times 10^{-3}$  at (9.1875, 0.2), while the maximum  $v$ -velocity in the secondary cell (and in the domain) is  $+4.441 \times 10^{-4}$  at (7.5, 0.6).

Plots of the solute concentration corresponding to Fig. 6 are shown in Fig. 7. As for the Bi-0.1 at.% Sn case, this plot for the richer alloy exhibits solute build-up near the interface, and the exponential profile characteristic of binary-alloy solute rejection. In Fig. 7 (a), close to the interface, the level of solute concentration increases with increasing  $y$ . Further from the solute interface, but still within the solute boundary layer, concentration increases with decreasing  $y$ , for a given  $x$  value. This is due to the localized convection in the positive  $y$  direction near the interface and the bulk thermally driven convection acting elsewhere (refer to Fig. 6a). At  $x = 3.1562$ , the maximum concentration is 4.559 at.% at  $y = 0.875$ , while the minimum value is 3.663 at.% at  $y = 0.175$ . Interface curvature effects are also evident, with the profile being preferentially rich away from the centerline ( $y = 0.5$ ).

As time progresses (Fig. 7b), the liquid becomes more solute-rich, with the maximum and minimum values near the interface ( $x = 5.2812$ ) being 7.205 at.% at  $y = 0.825$  and 4.747 at.% at  $y = 0.175$ , respectively. The additional solute rejected and stronger solutal convection (see Fig. 6b) have led to higher levels of solute segregation in the  $y$ -direction when compared to Fig. 7 (a). The higher levels of solute rejection and solutal convection in the liquid will cause higher levels of segregation in the solid. Figure 7 (c) is a plot of liquid solute concentration after 2.90 hours. The general character of the profile has changed slightly. The existence of the secondary cell has decreased the level of convection in the negative  $y$ -direction in the outer regions of the boundary layer. Close to the interface, the strong positive vertical velocities have led to increased solute build-up at large  $y$ . The maximum and minimum values of interfacial liquid solute concentration ( $x = 7.4062$ ) are 9.682 at.% at  $y = 0.875$  and 5.423 at.% at  $y = 0.175$ , respectively. Note that concentration values of this magnitude would be sufficient to lower the melting temperature of the alloy by a significant amount (see Simpson et al. 1998). This implies that the assumption that the melting temperature remains constant is not valid. The likely effect of concentration-dependent melting temperature would be to cause the interface to be thicker near the bottom of the domain. This effect may alter the concentration and velocity fields and will be addressed in future work.

For the higher alloy concentrations, solutal convection plays a much larger role, as can be seen in the concentration profiles discussed above. As the growth proceeds, the level of solutal convection grows, with a corresponding change in the solute distribution. The maximum concentration increases much more rapidly than the minimum value.

## CONCLUSIONS

A series of fully transient simulations of horizontal Bridgman crystal growth in microgravity conditions have been performed. The pure bismuth simulation was found to agree well with a similar simulation of the process (Yao et al. 1997), in terms of the convection level and the

presence of slight interface curvature.

For the dilute alloy simulation (Bi-0.1 at.% Sn), a single dominant counter-clockwise rotating convective cell is present for the entire duration of the process. As time proceeds, solute is rejected at the interface and the level of solute near the interface increases. Due to the presence of convection, radial solute segregation occurs with preferentially higher values at the bottom of the domain. It is unclear if the level of segregation increases with time. The maximum values of concentration are small and so the assumption of constant alloy melting temperature is realistic.

For the richer alloy (Bi-1.0 at.% Sn), the convective field is much more complex. Higher levels of solute rejection at the interface cause higher levels of solutal convection. Initially, a single, thermally driven, counter-clockwise rotating cell is present. As time proceeds and solute accumulates at the interface, a secondary, solute driven clockwise rotating cell develops. The effect of this convective pattern is to yield significant levels of segregation in the solute near the interface (and hence in the solid). This segregation is such that the values near the top of the domain are maximum. The higher values of concentration near the interface would result in a significant change in the melting temperature for the alloy. Thus the assumption that the melting temperature is constant is not valid for this case. Investigating the effects of concentration-dependent melting temperature will be addressed in future work. A comparison of results with existing microgravity experimental data and a further series of simulations for Bridgman growth of succinonitrile (Yao and de Groh, 1993) under terrestrial and microgravity conditions are also planned as future work.

## Acknowledgments

Partial funding for this work from NASA (Coop. Agreement # NCC3-557) is gratefully acknowledged. JES was funded by a UW-Milwaukee Graduate School Fellowship. The insightful help of Dr. M. Yao of the Ohio Aerospace Institute is much appreciated. Professors G. de Vahl Davis and E. Leonardi and Dr. V. Timchenko of the University of New South Wales are particularly thanked for kindly providing their code, FRECON3V, which was the starting point for this work.

## REFERENCES

- Abbaschian, R., Gokhale, A. B., Favier, J. J. and Coriell, S. R., 1992, In-Situ Monitoring of Crystal Growth Using MEPHISTO, NASA Science Requirements Document (SRD).
- Abbaschian, R., 1996, In-Situ Monitoring of Crystal Growth Using MEPHISTO: Revised Science Requirements Document (RSRD) for the Re-flight of MEPHISTO aboard USMP-4.
- Adomato, P. M. and Brown, R. A., 1987, Convection and segregation in directional solidification of dilute and non-dilute binary alloys, *J. Crystal Growth*, Vol. 80, pp. 155-190.
- Alexander, J. I. D., Ouazzani, J. and Rosenberger, F., 1989, Analysis of the low gravity tolerance of Bridgman-Stockbarger crystal growth, *J. Crystal Growth*, Vol. 97, pp. 285-302.
- Alexiades, V. and Solomon, A. D., 1993, *Mathematical Modeling of Melting and Freezing Processes*, Hemisphere, Washington D.C.
- Barrett, R., Berry, M., Chan, T. F., Demmel, J., Donato, J. M., Dongarra, J., Eijkhout, V., Pozo, R., Romine, C. and Van der Vorst, H., 1994, *Templates for the Solution of Linear Systems: Building Blocks for Iterative Methods*, SIAM, Philadelphia.
- de Groh III, H. C. and Nelson, E. S., 1994, On residual acceleration during space experiments, *Heat Transfer in Microgravity Systems*, ASME HTD-Vol. 290, pp. 23-33.

de Groh III, H. C. and Yao, M., 1994, Numerical and experimental study of transport phenomena in directional solidification of succinonitrile, *Transport Phenomena in Solidification*, ASME HTD-Vol 284, pp. 227-243.

Garimella, S. V. and Simpson, J. E., 1998, Interface propagation in the processing of metal matrix composites, *Microscale Thermophysical Engineering* (in press).

Hirt, C. W. and Nichols, B. D., 1981, Volume of fluid (VOF) method for the dynamics of free boundaries, *J. Comp. Phys.*, Vol. 39, pp. 210-225.

Kurz, W. and Fisher, D. J., 1989, *Fundamentals of Solidification*, Trans Tech Publications.

Liang, M. C. and Lan, C. W., 1996, Three-dimensional convection and solute segregation in vertical Bridgman crystal growth, *J. Crystal Growth*, Vol. 167, pp. 320-332.

Mallinson, G. D. and de Vahl Davis, G., 1973, The method of the false transient for the solution of coupled elliptic equations, *J. Comput. Phys.*, Vol. 12, pp. 435-461.

Raw, W. Y. and Lee, S. L., 1991, Application of weighting function scheme on convection-conduction phase change problems, *Int. J. Heat Mass Transfer*, Vol. 34, pp. 1503-1513.

Roache, P. J., 1976, *Computational Fluid Dynamics*, Hermosa.

Samarskii, A. A. and Andreyev, V. B., 1963, On a high-accuracy difference scheme for an elliptic equation with several space variables, *USSR Comput. Math. and Math. Phys.*, Vol. 3, pp. 1373-1382.

Simpson, J. E. and Garimella, S. V., 1997, Melt convection and front propagation in the unidirectional solidification of a pure material, *Procs. 4th Decennial Int. Conf. Solidification Processing*, Sheffield, UK, J. Beech and H. Jones (Eds.), pp. 130-134.

Simpson, J. E. and Garimella, S. V., 1998, An investigation of the solutal, thermal and flow fields in unidirectional alloy solidification, *Int. J. Heat Mass Transfer* (in press).

Simpson, J. E., Yao, M., de Groh III, H. C. and Garimella, S. V., 1998, Numerical modeling of solidification in space with MEPHISTO-4 (Part 2), NASA Technical Memorandum TM-1998-206630.

Timchenko, V., Leonardi, E. and de Vahl Davis, G., 1997, FRECON3V User's Manual, University of New South Wales, School of Mechanical and Manufacturing Engineering, Report 1997/FMT/1, and FRECON3V Programmer's Manual, Report 1997/FMT/2.

Yao, M. and de Groh III, H. C., 1993, Three-dimensional finite element method simulation of Bridgman crystal growth and comparison with experiments, *Num. Heat Transfer, Part A*, Vol. 24, pp. 393-412.

Yao, M., de Groh III, H. C. and Abbaschian, R., 1997, Numerical modeling of solidification in space with MEPHISTO-4 (Part 1), *35<sup>th</sup> Aerospace Sciences Meeting and Exhibit*, Reno, NV, Paper AIAA 97-0449.

Yao, M., Raman, R. and de Groh III, H. C., 1995, Numerical simulation of heat and mass transport during space crystal growth with MEPHISTO, NASA Technical Memorandum 107015.